energies

Article

Effects of Liquid Density on the Gas-Liquid Interaction of the Ionic Liquid Compressor for Hydrogen Storage

Yi Guo [1], Qi Wang [1], Maofei Geng [2], Xueyuan Peng [1,*] and Jianmei Feng [1]

1 School of Energy and Power Engineering, Xi'an Jiaotong University, Xi'an 710049, China
2 State Key Laboratory of Compressor Technology (Anhui Laboratory of Compressor Technology), Hefei 230031, China
* Correspondence: xypeng@mail.xjtu.edu.cn

Abstract: As a new and promising compression technology for hydrogen gas, the ionic liquid compressor inherits the advantages of the ionic liquid and the hydraulic system. The liquid density is one of the key parameters influencing the fluid flow field, the sloshing of the bulk liquid, and the movement of droplets generated during the compressor operation. An appropriate selection of the liquid density is important for the compressor design, which would improve the thermodynamic performance of the compressor. However, the density of the ionic liquid varied significantly depending on the specific combination of the cation and anions. This paper proposed the methodology to select the optimal liquid density used in the ionic liquid compressor for hydrogen storage. The gas-liquid interaction in the compression chamber is analysed through numerical simulations under varied liquid density values. Results found that the increase in the liquid density promoted the detachment of the ionic liquid from the cylinder cover during the suction procedure and the contact of the bulk liquid on the compressor cover when the gas is compressed in the cylinder during the compression procedure. Both the droplet size and the dimension of the derived gas vortex decreased when the liquid density increased. The lowest mass transfer of hydrogen through the outlet was obtained at the density of 1150 kg/m^3. The density of the ionic liquid from 1300 to 1450 kg/m^3 is suggested to the hydrogen compressor, taking into account the transient two-phase flow characteristics, the mass transfer, and the total turbulent kinetic energy.

Keywords: hydrogen energy; gas-liquid interaction; ionic liquid compressor; density influence; CFD simulation

check for updates

Citation: Guo, Y.; Wang, Q.; Geng, M.; Peng, X.; Feng, J. Effects of Liquid Density on the Gas-Liquid Interaction of the Ionic Liquid Compressor for Hydrogen Storage. *Energies* **2023**, *16*, 3193. https://doi.org/10.3390/en16073193

Academic Editor: Silvia Ravelli

Received: 2 March 2023
Revised: 24 March 2023
Accepted: 28 March 2023
Published: 1 April 2023

1. Introduction

The urgent desire for renewable energy has become a worldwide concern due to the rising population, the near exhaustion of fossil fuels, and environmental pollution issues [1]. Hydrogen is regarded as a promising transition medium [2], which is considered an effective solution to abate the emission of greenhouse gas [3] because of its abundant production ways [4], vast demand in the industry field [5], high specific energy density [6], and abundance in various forms [7]. The automobile driven by electrical energy is also a significant technology for renewable energy applications [8]. As it was reported that 30% of the total greenhouse gas emission comes from the transportation sector [9], the hydrogen fuel cell vehicle (HFCV) is, therefore, an effective application of hydrogen energy [10]. However, the development and application of HFCVs confront a challenge due to the requirement of large volumetric density in a small space [11], high cost in the infrastructure institutes [12], and sparse distribution of refuelling sites [13].

As the energy density per volume of hydrogen is only 0.03% of the gasoline at ambient pressure [14] and 14% of the natural gas [15], a large storage space is required for the application of hydrogen fuel, which consequently increases the costs of the hydrogen refuelling station and the fuel price [16]. The hydrogen storage methods can be classified as compressed gas storage, cryogenic hydrogen storage, cryo-compressed hydrogen storage, and material-based hydrogen storage. The compressed gas storage of hydrogen in a vessel is the widely accepted form in HFCVs, where the pressure of hydrogen is required as 45 MPa (for the 35 MPa refuelling station) or 90 MPa (for the 70 MPa refuelling station) [17]. Cryogenic and cryo-compressed hydrogen storage are applied when hydrogen is transported over a long distance, where the hydrogen is stored in the liquid phase at the cryogenic temperatures of 20 K, which is more costly than the compressed gas technology in the short-distance hydrogen refuelling stations due to the significant energy for the liquefaction of hydrogen [18]. The material-based hydrogen storage depends on the pore material, which is costly to manufacture and lacks the technical information for high-pressure applications [19].

Compressors applied in the HFCVs, including ones for hydrogen and air. Turbo compressors are kinetic types that are suitable for gas with large molecules and are, therefore, always applied for supplying the air to the fuel cell stack [20]. In terms of hydrogen, compressed hydrogen gas is an effective means of hydrogen storage because of the enlarged volumetric energy density with the increase in hydrogen pressure for storage in the hydrogen refuelling station [21]. Numerous compression technologies are, therefore, investigated for the hydrogen refuelling station, which includes the positive displacement type such as the diaphragm compressor [22], the ionic liquid compressor [23], the reciprocating piston compressor [24], as well as the chemical-physical type, such as the metal hydride compressor [25] and adsorption compressor [26]. Key parameters such as the hydrogen flow rate, hydrogen temperature, hydrogen pressure, compression ratio, and hydrogen purity need to be taken into account when selecting the appropriate type of hydrogen compressor.

Among different types of compression technologies, the diaphragm and metal hydride compressors are the most popular form for researchers. Hu et al. [27] proposed a new generatrix for the cavity profile of the diaphragm compressor to reduce the radial stresses of the diaphragm. It was reported that the new profile was able to decrease the maximal and the centric radial stress of the diaphragm by 8.2% and 13.9%, respectively. Ren et al. [28] theoretically and experimentally investigated the volumetric efficiency of the diaphragm compressor for hydrogen gas, considering the effect of hydraulic oil compressibility. It was found that hydraulic oil compressibility was a key parameter generating a loss of 37% of volumetric efficiency. Wang et al. [29] analysed the deformation stress of the diaphragm compressor cylinder head under high temperature and high pressure. It proposed an improvement on the structure to reduce the stress of the discharge hole, which successfully reduced the stress and guaranteed the safe operation of the diaphragm compressor. In terms of the metal hydride compressor, Peng et al. [30] proposed a three-stage metal hydride hydrogen compressor where different materials are applied in different stages. It was found by the theoretical analysis that LaNi5-based alloys exhibit excellent application prospects in high-density hydrogen storage and primary hydrogen compression materials. Grey [31] developed a thermodynamic model for the selection of hydrogen storage alloys applied in the multi-stage metal-hydride compressor. The proposed model was derived from the first principle based on the van 't Hoff relation. It was found that the proposed model was only valid at high hydrogen pressures. Gkanas et al. [32] compared the compression ratio, the flow rate of hydrogen, thermal energy consumption, and compressor efficiency of four different metal hydride compressors. The optimal type of compressor was identified for the compression in the temperature range of 10–90 °C with an isentropic efficiency of 4.54% and a thermal energy consumption of 322 kJ/mol hydrogen.

By combining the liquid piston compression and the hydraulic system, the ionic liquid compressor shows a new way to compress hydrogen gas [33], where the ionic liquid is adopted and located in the gas compression cylinder [34]. The ionic liquid is the salt with a melting temperature lower than 100 °C presenting as a liquid at room temperature [35]. The ionic liquid typically consists of large and unsymmetrical organic cations and polyatomic organic or inorganic anions [36]. The ionic liquid can be categorised into eleven groups, including acidic ionic liquid, basic ionic liquid, neutral ionic liquid, functionalized ionic liquid, protic ionic liquid, etc. [37]. The thermophysical properties of the ionic liquid, such as the density, viscosity, and surface tension, can be changed by adjusting the cation and anion constituents. Therefore, one of the famous features of the ionic liquid is its 'designability' as there are a huge number of ion combinations and the possibility of designing the target-pointing ionic liquid [38].

In the ionic liquid compressor, the ionic liquid is applied as a liquid piston above the solid piston to separate the hydrogen gas and the solid piston. Due to the existence of the ionic liquid, it can work as a liquid sealing and the lubricant between the solid piston and the compression chamber. The ionic liquid compressor is an effective method for compressing hydrogen because of the inherent advantages of the ionic liquid, for instance, the extremely low vapour pressure [39], the excellent lubricity feature [40], inert features in thermal [41] and chemical [42] reactions, and nonflammability [43]. It is worth noting that the ionic liquid compressor is applied for the onsite compression and storage of hydrogen in the hydrogen refuelling stations, which is not designed for long-distance transporting. Additionally, a complex gas-liquid interaction in the compression chamber would occur due to the existence of the ionic liquid in the cylinder. During the suction and discharge procedure, the fluid field near the inlet and outlet orifices would influence the internal flow field in the compression chamber, which further impacts the free face of the bulk liquid. When the interface shape changes, it may generate droplets in the gas space or entrainment gas in the bulk liquid.

According to the Navier-Stokes momentum equation, the flow velocity is closely related to the fluid density [44]. In the gas-liquid two-phase system, a significant shear at the interface would be generated because of the large density ratio in the multiphase flow system [45]. The large density ratio in the compression cylinder is one of the specific features of the ionic liquid compressor because of the relatively high value in the liquid density and the extremely low density of the hydrogen gas. The density ratio is a key parameter when the sloshing phenomenon is in consideration [46], which, therefore, should be taken into account when designing the ionic liquid compressor. Moreover, Yong et al. [47] argued that the settling of a particle in the static flow in the vertical channel is a challenging issue due to the complex interaction of the dynamic movement particle and the flow pattern. Their study showed that different density ratios led to different sedimentation behaviours of the particle. Therefore, in the ionic liquid compressor, it can be inferred that the movement of the generated liquid droplet is dependent on the liquid density as it is in a nonstatic flow system which results in a much more complex environment in the cylinder. To sum up, in this gas-liquid two-phase system, the liquid density would influence the fluid flow velocity, the dynamic characteristics of the interface, and the movement of the droplet.

Therefore, it can be concluded that the liquid density is one of the key parameters influencing the fluid flow field, the sloshing of the bulk liquid, and the movement of droplets generated during the compressor operation. This would further influence the thermodynamic progress of the ionic liquid compressor. The density of the ionic liquid varied from 983–1660 kg/m^3 only for the imidazolium-based ionic liquid, according to the public literature [48–51]. An appropriate selection of the liquid density is therefore important for the compressor design, which would improve the thermodynamic performance of the ionic liquid compressor.

In this study, the methodology of selecting the liquid density for designing the hydrogen compressor was proposed. The effects of the liquid density on the dynamic characteristics of the gas-liquid interface, the transferred mass through the outlet, and the total turbulent kinetic energy were analysed, based on which the optimal liquid density was obtained.

2. Methodology

This paper focuses on the design of the compressor applied in the hydrogen refuelling station. Therefore, some assumptions related to hydrogen production have to provide for the study. Major assumptions are shown as follows.

(1) Hydrogen gas is regarded as with a high purity without the water content.

(2) Inlet hydrogen temperature is assumed as the environment temperature.
(3) Hydrogen production methods are not considered in the study, which means that the hydrogen colour type is not taken into account.

The methodology for the investigation of the effects of liquid density on the dynamic behaviour of the interface in the gas-liquid two-phase system for designing the ionic liquid compressor servicing the refuelling of hydrogen fuel is provided in Figure 1. The methodology mainly consists of three parts. Part 1 is the structure design, which aims to fulfil the function of compressing the hydrogen gas in the working principle. Part 2 and Part 3 are the numerical simulation and density selection, respectively. The functional design of the compressor for hydrogen compression is provided in Figure 2. The compressor contains the valves, the gas compression and hydraulic oil chambers, the ionic liquid and solid pistons piston, and the hydraulic oil channel. The transferred hydrogen gas transfers via the inlet valve in the gas compression cylinder by increasing the chamber volume. When the chamber volume is reduced, the hydrogen pressure is elevated inside. Ideally, when the gas pressure is higher than that in the discharge channel, the discharge valve opens, and the hydrogen gas flows out of the compression cylinder through the discharge valve. The solid piston in the cylinder chamber is forced by the hydraulic oil provided by a hydraulic system, consequently driving the reciprocating motion of the bulk liquid located on top of it.

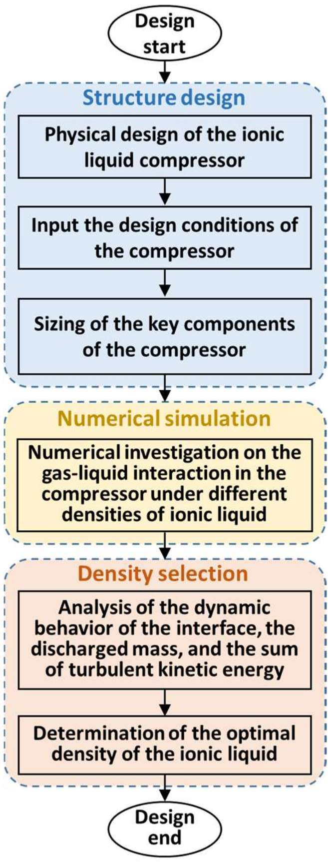

Figure 1. Methodology of density selection for the hydrogen compressor design.

After the physical design is finished, the sizes of the major components of the gas compression part are determined according to the design requirements. The requirements for designing the hydrogen compressor adopting the bulk ionic liquid are summarized in Table 1. The inlet condition of the hydrogen gas is a pressure of 12 MPa and a temperature of 25 °C. The outlet requirement of the hydrogen gas for the design is a pressure of 45 MPa, which indicates a compression ratio of 3.75. Therefore, the compressor is designed as one stage for hydrogen compression. The flow rate requirement of the compressor is 150 Nm^3/h with a reciprocating frequency of 5 Hz. The numerical model for simulating the gas-liquid interaction inside the gas compression cylinder is then developed according to the calculated structural size. Simulations with different density values of the ionic liquid are then carried out, as presented in Table 2. According to the study of Fredlake et al. [52], Lazzús [49], Gardas et al. [50], and Tome et al. [51], it was concluded that the density of imidazolium-based ionic liquids is mainly in the range of 983–1660 kg/m^3. Therefore, 5 simulations are conducted at the density of 1000, 1150, 1300, 1450, and 1600 kg/m^3, separately. Other thermophysical properties are set based on the ionic liquid of [EMIM][Tf2N] [53]. The results of simulations are then analysed to determine the optimal liquid density considering the dynamic behaviour of the gas-liquid interface, the transferred mass through the outlet valve, and the total turbulent kinetic energy.

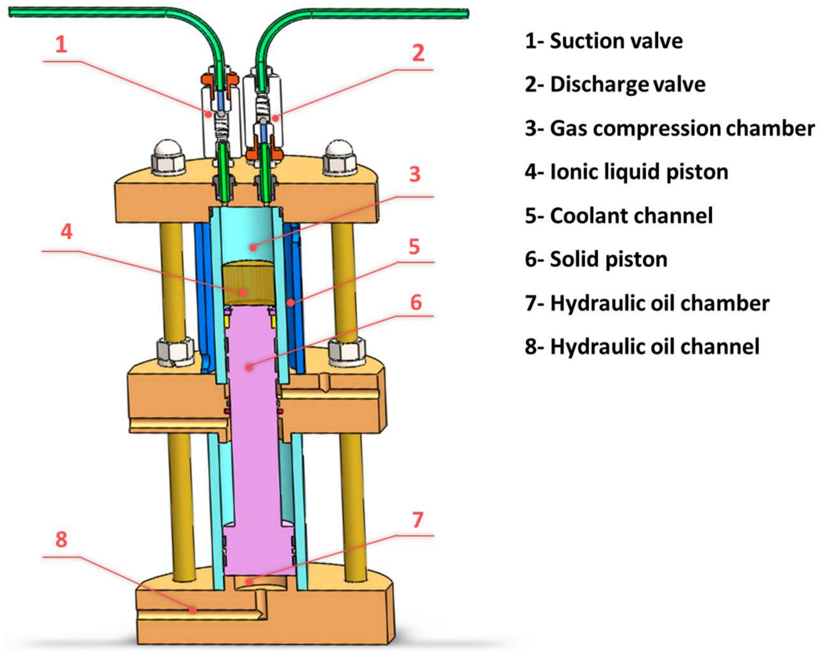

Figure 2. Physical structure of hydrogen compressor.

Table 1. Requirements for designing the hydrogen compressor in this study.

Inlet Condition		Outlet Condition		Working Specification	
Pressure (MPa)	Temperature (°C)	Pressure (MPa)	Compression Ratio	Flow Rate (Nm^3/h)	Frequency (Hz)
12	25	45	3.75	150	5.0

Table 2. Information on the ionic liquid properties in the hydrogen compressor.

No.	Thermophysical Properties			
	Density (kg/m^3)	Dynamic Viscosity (mPa·s)	Thermal Conductivity (W/m·K)	Heat Capacity (J/mol·K)
1	1000	51.87	0.1209	509.2
2	1150	51.87	0.1209	509.2
3	1300	51.87	0.1209	509.2
4	1450	51.87	0.1209	509.2
5	1600	51.87	0.1209	509.2

3. Mathematical and Numerical Model

3.1. Computational Domain and Size Calculation

The computational domain for the gas compression part is illustrated in Figure 3, which contains the clearance volume due to the valve structure, the gas compression region, and the bulk ionic liquid. As this study aims to study the gas-liquid interaction, a boundary condition of the moving wall is set to represent the top surface of the solid piston. Therefore, the key sizes for the simulation are the diameter of the cylinder for hydrogen gas compression, the diameter of the suction and discharge orifices, and the stroke of the solid piston.

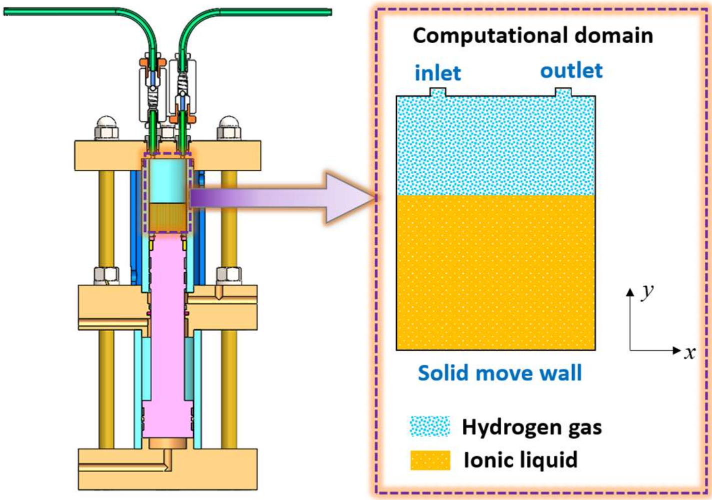

Figure 3. Computational domain in the numerical model.

The diameter of the cylinder for hydrogen gas compression is calculated as:

$$D = \sqrt[3]{\frac{4V_{\mathrm{st}}}{60\pi r f}}, \tag{1}$$

where D is the cylinder diameter; r is the ratio of the stroke to diameter for the compression cylinder, which is set as 1.0 in this study; f is the frequency of reciprocating motion; V_{st} is the one-stroke volume in the compressor cylinder, which can be calculated as:

$$V_{\mathrm{st}} = \frac{F_{\mathrm{in}}}{\lambda_{\mathrm{d}}}, \tag{2}$$

where F_{in} is the volumetric flow rate through the inlet valve; λ_{d} is the discharge coefficient. F_{in} and λ_{d} are obtained as:

$$F_{\mathrm{in}} = \frac{F_0}{60} \times \frac{p_0}{p_{\mathrm{in}}} \times \frac{T_{\mathrm{in}}}{T_0}, \tag{3}$$

$$\lambda_{\mathrm{V}} = 1 - r_{\mathrm{CV}}\left(\varepsilon_c^{\frac{1}{k\mathrm{e}}} - 1\right), \tag{4}$$

$$\lambda_{\mathrm{d}} = \lambda_{\mathrm{V}}\lambda_{\mathrm{p}}\lambda_{\mathrm{T}}\lambda_{\mathrm{l}}, \tag{5}$$

where 0 represents the standard condition while in indicates the inlet term; p and T are pressure and temperature, respectively; λ is the required coefficient for size calculation; the subscripts V, p, T, and l denote the coefficient related to the volume, pressure, temperature, and leakage sources; r_{CV} and are the clearance volume and expansion coefficients, respectively; ε_c is the compression ratio.

The diameter of valves is obtained based on the effective flow area A_{e}, which can be obtained as:

$$A_{\mathrm{e}} = \frac{A_{\mathrm{p}}}{N v_{\mathrm{vm}}} v_{\mathrm{m}}, \tag{6}$$

where A_{p} is the area of the piston cross-section; N stands for the valve number at the inlet/outlet; v_{vm} is the gas average velocity in the clearance space of valves; v_{m} is the mean velocity of the reciprocating motion of the piston calculated based on the Mach number M and the sound velocity a as described by:

$$v_{\mathrm{vm}} = Ma, \tag{7}$$

3.2. Governing Equations

The volume fraction in each control cell is calculated by the VOF method, which is implemented in the software of ANSYS Fluent. The VOF method is able to track the movement of the interface in the gas-liquid two-phase system, the governing equations of which are shown as follows.

Continuity equation:

$$\frac{\partial(\alpha_z \rho_z)}{\partial t} + \nabla\cdot(\alpha_z \rho_z \boldsymbol{u}) = 0, \tag{8}$$

where z indicates the zth phase; t is the time; α stands for the volume ratio of a specific phase; ρ indicates the density of each phase; $\boldsymbol{u}$ is the vectorial term of the velocity.

The velocity vector of the gas-liquid mixture is determined as:

$$\boldsymbol{u} = \frac{\sum_{a=0}^{a=z} \alpha_z \rho_z \boldsymbol{u}_z}{\sum_{a=0}^{a=z} \alpha_z \rho_z}, \tag{9}$$

The sum of volume ratios of all phases in each calculation element is 1, which is described as:

$$\sum_{a=0}^{a=z} \alpha_z = 1, \tag{10}$$

Momentum equation:

$$\frac{\partial(\rho \boldsymbol{u})}{\partial t} + \nabla\cdot(\rho \boldsymbol{u}\boldsymbol{u}) = -\nabla p + \nabla\cdot\left[\mu\left(\nabla \boldsymbol{u} + \nabla \boldsymbol{u}^{\mathrm{T}}\right)\right] + \rho \mathbf{g} + \boldsymbol{F}, \tag{11}$$

where $\mathbf{g}$ and $\boldsymbol{F}$ are the vectorial terms of the gravity acceleration and external force, respectively; μ is the viscosity.

Energy equation:

$$\frac{\partial(\rho h)}{\partial t} + \rho v\cdot\nabla h = \nabla(\lambda \nabla \mathrm{T}), \tag{12}$$

where v is the velocity; λ is the thermal conductivity.

In each calculation element, the properties of fluids are the combination of the corresponding properties of all phases, which are described as:

$$\rho = \sum_{a=0}^{a=z} \alpha_z \rho_z, \tag{13}$$

$$\mu = \sum_{a=0}^{a=z} \alpha_z \mu_z, \tag{14}$$

$$\lambda = \sum_{a=0}^{a=z} \alpha_z \lambda_z, \tag{15}$$

3.3. Boundary Conditions and Calculation Setting

Boundary conditions that need to be set in the simulation are the inlet, outlet, solid move wall, and the rest surfaces, as shown in Figure 3. Simulation settings at the inlet and outlet boundaries are illustrated by Equations (16) and (17), respectively, by inputting a user-defined function (UDF) in Fluent.

$$\begin{cases} \text{Wall, } p > 12 \text{ MPa} \\ \text{Pressure inlet (12 MPa), } p \leq 12 \text{ MPa} \end{cases}, \quad (16)$$

$$\begin{cases} \text{Wall, } p \leq 45 \text{ MPa} \\ \text{Pressure outlet (45 MPa), } p > 45 \text{ MPa} \end{cases}, \quad (17)$$

Dynamic mesh is set on the solid move wall by UDF based on Equation (18).

$$v = -2\pi f \frac{S}{2} \sin(2\pi f t), \quad (18)$$

The rest surfaces are set as adiabatic walls. The standard $k - \varepsilon$ model in simulations can be illustrated by Equations (19) and (20), which show the relationship between the dissipation rate in the turbulence flow ε and the turbulent kinetic energy of turbulence flow k.

$$\frac{\partial}{\partial t}(\rho k) + \frac{\partial}{\partial x_i}(\rho k u_i) = \frac{\partial}{\partial x_j}\left[\left(\mu + \frac{\mu_t}{\sigma_k}\right)\frac{\partial k}{\partial x_j}\right] + G_k + G_b - \rho\varepsilon, \quad (19)$$

$$\frac{\partial}{\partial t}(\rho \varepsilon) + \frac{\partial}{\partial x_i}(\rho \varepsilon u_i) = \frac{\partial}{\partial x_j}\left[\left(\mu + \frac{\mu_t}{\sigma_\varepsilon}\right)\frac{\partial \varepsilon}{\partial x_j}\right] + C_{1\varepsilon}\frac{\varepsilon}{k}(G_k + C_{1\varepsilon}G_b) - C_{2\varepsilon}\rho\frac{\varepsilon^2}{k}, \quad (20)$$

where G_k is the kinetic energy generated because of the difference in the velocity field; G_b is the turbulent kinetic energy generated because of the buoyance; C is the constant for calculation; σ_k and σ_ε are the Prandtl number and the viscosity to dissipation diffusion ratio, respectively.

Taking into account the calculation speed and the design target, simulations of the gas-liquid interaction in the compression chamber during one entire compression operation are carried out through the 2D transient numerical model. The simulation time is 0.2 s, which is determined based on the working frequency. The initial temperature in the fluid domain is set as 25 °C while the initial pressure is set as 45 MPa.

3.4. Independence Verification of the Mesh Size and Time Step

Simulations with the liquid properties of [EMIM][Tf2N] with different mesh sizes and time steps were performed to verify the independence of these setting values. The results of the simulations are summarised in Table 3. It was found that the largest errors were obtained as 2.10% and 1.99% for the mesh size and time step, respectively. Thus, the numerical simulations in this paper were all conducted under the mesh size of 0.5 mm with a time step of 1×10^{-4} s.

Table 3. Results of simulations under the different mesh and time settings.

	Mesh Size (mm)				**Time Step (s)**		
Value	0.7	0.6	0.5	0.4	2×10^{-4}	1×10^{-4}	0.5×10^{-4}
Discharged mass (g)	14.50	14.84	14.81	14.56	15.11	14.81	14.78
Deviation (%)	2.10	0.22	/	1.71	1.99	/	0.22

4. Results and Discussion

4.1. Results of the Size Calculation

Based on the size design, the orifice dimension at the inlet and outlet was obtained as 0.004 m for the diameter, while the size of the lift limiter was 0.002 m. The cylinder size in the compressor was obtained with a diameter of 0.05 m, which was the same as the stroke of the reciprocating motion. The void fraction at the beginning of the compression cycle was then obtained as 0.0512% based on the geometry information. Numerical simulations under different liquid densities were then carried out based on these size results.

4.2. Results of the CFD Simulations

An entire compression cycle is composed of four processes, including clearance volume expansion, hydrogen gas suction, hydrogen gas compression, and gas discharge procedures. As presented in Figure 4, the characteristic moments of gas-liquid interaction during one-cycle compression under the liquid density of 1000 kg/m^3 were summarised and grouped into two stages. Stage I contained the clearance gas expansion and hydrogen gas suction procedures, while Stage II consisted of the hydrogen gas compression and discharge procedures. During the suction procedure, the gas flowed into the gas compression cylinder and formed a relatively large gas space at the suction side, as shown in the snapshot of 0.0250 s. Due to the adhering of the liquid on the cylinder cover, the gas space at the suction side is not connected to that at the discharge side. A gas vortex induced by the suction gas flow was revealed at the time of 0.0250 s, as shown in Figure 4b. The vortex dimension enlarged with time in Stage I. At 0.0700 s, two derived vortexes were observed, the large one of which is located below the original vortex, while the small one is located next to the original one at the discharge side. A wave with two peaks was generated at the time of 0.0560 s, which generated one droplet from the wavefront at 0.1000 s. A droplet of the liquid adhered on the side wall can be observed at 0.0700 s, while two droplets were generated from the liquid film at 0.1000 s. A neck phenomenon was found at 0.1000 s in the bulk ionic liquid at the location of the original liquid level due to the action of the largely derived vortex. There are a total of three liquid drops produced in Stage I. All of them were transferred and integrated into the bulk liquid, as shown in the picture at 0.1600 s. The wave with two peaks disappeared at 0.1300 s when a lump-like wave was generated and moved to the cylinder cover. As presented in Figure 4b, the dimension of all gas vortexed reduced with time. The largely derived gas vortex was forced to the outlet region due to the wave shifting, while the small one almost disappeared at 0.1300 s. No vortex was observed at 0.1600 s. During the discharge procedure, the ionic liquid flowed out of the compression chamber together with the hydrogen gas, which can be clearly observed at 0.1755 s. At 0.2000 s, the ionic liquid blocked the discharge channel and trapped hydrogen gas inside located close to the chamber wall. The gas space near the outlet region was bigger than the inlet site at the end of Stage II. The highest gas velocity was observed as 11 m/s at 0.0560 s in Stage I and 19.6 m/s at 0.1755 s in Stage II.

The transient gas-liquid interaction in one entire operation cycle with a liquid density of 1150 kg/m^3 is presented in Figure 5. Similarly to that with the density of 1000 kg/m^3, the gas space was formed and increased at the suction side during the suction procedure. The wave with two peaks was revealed in the clearance volume expansion process. A droplet was produced from the ionic liquid adhered to the side wall at 0.0700 s, which moved to the middle of the cylinder at 0.1000 s. A connection between the gas regions near the inlet and outlet sides was found at 0.0700 s. Three droplets were generated at 0.1000 s, one of which was produced from the wavefront. This wavefront-generated droplet was smaller than the liquid density of 1000 m^3/s. As displayed in Figure 5b, the gas vortex was produced due to the gas flow near the inlet, which induced two derived vortexes. The larger derived vortex forced one of the droplets to float in the gas space. Due to the force of the largely derived gas vortex, a neck part was also observed in the bulk liquid at the original liquid surface level, the thickness of which was larger compared to that in the case of 1000 kg/m^3. At the time of 0.1300 s, two of the droplets integrated into the bulk liquid, which is different from the density of 1000 kg/m^3. It was found that the generated drops integrated into the bulk liquid early compared to 1000 kg/m^3. It can be seen that at 0.1600 s, the last and biggest droplet was integrated into the bulk liquid, the location of which was found rightwards compared to 1000 kg/m^3. The generated vortexes were found to disappear at 0.1600 s. At 0.1671 s, it can be seen that the ionic liquid transferred out with the gas together at the outlet. When the operation was close to the end of Stage II, gas-occupied space inside the bulk liquid was observed because of the blocking in the outlet channel by the liquid phase. The peak values of the velocity in Stages I and II occurred at 0.0582 and 0.1671 s, respectively. The largest velocity in Stage I was found as 10.8 m/s which was slightly lower than that in the case with the liquid density of 1000 kg/m^3. The highest velocity in Stage II was observed as 23.3 m/s, which was higher than that in the simulation under the liquid density of 1000 kg/m^3.

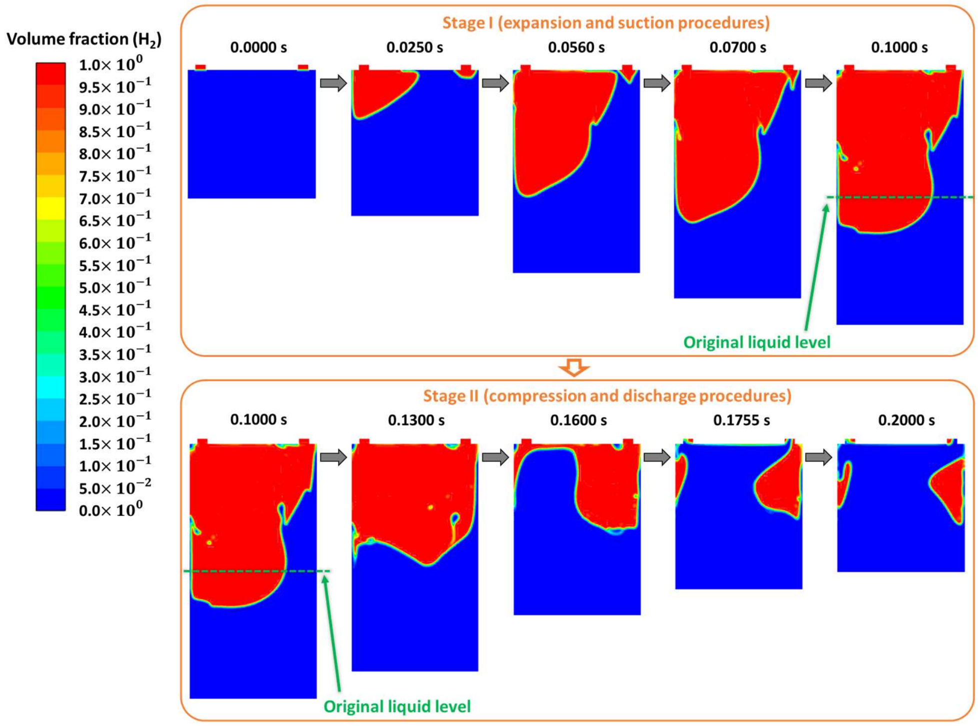

(a)

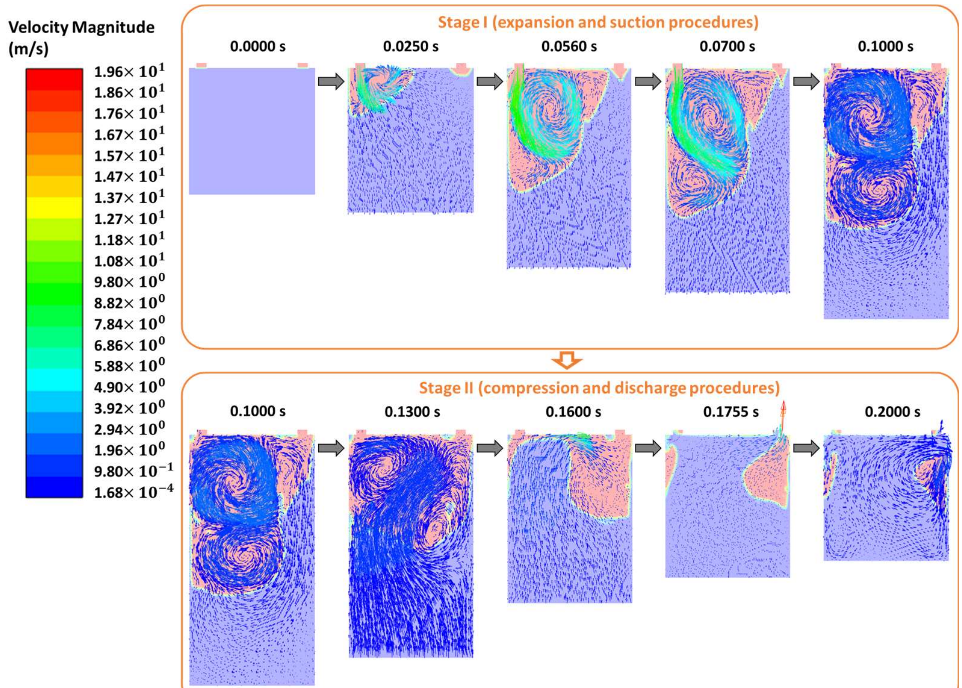

(b)

Figure 4. Results of the (**a**) volume fraction distribution and (**b**) velocity distribution (density of the ionic liquid: 1000 kg/m^3).

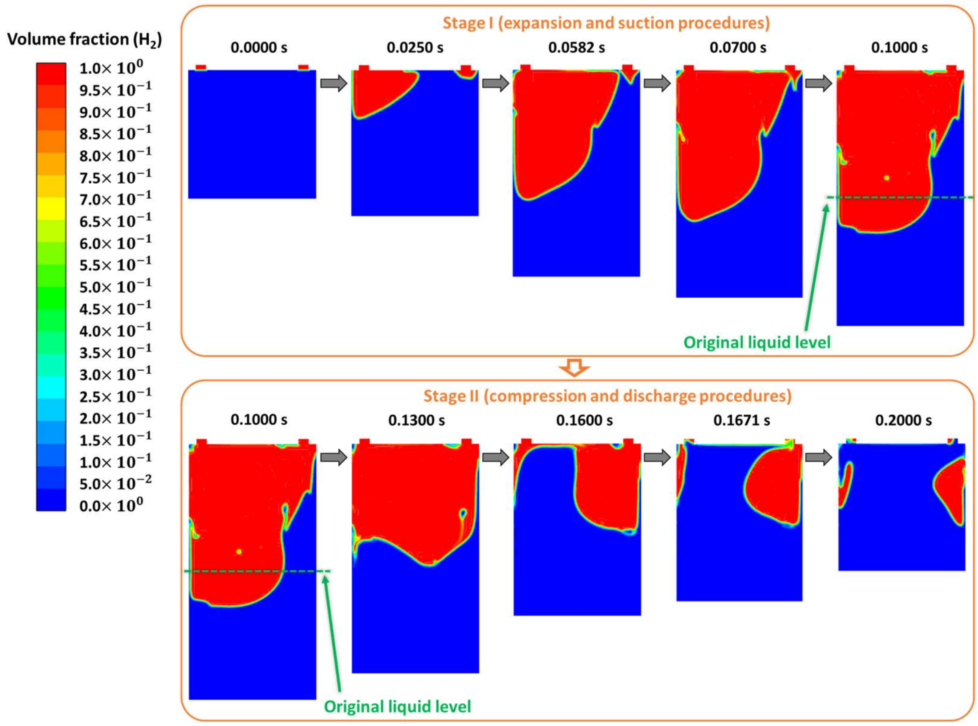

(a)

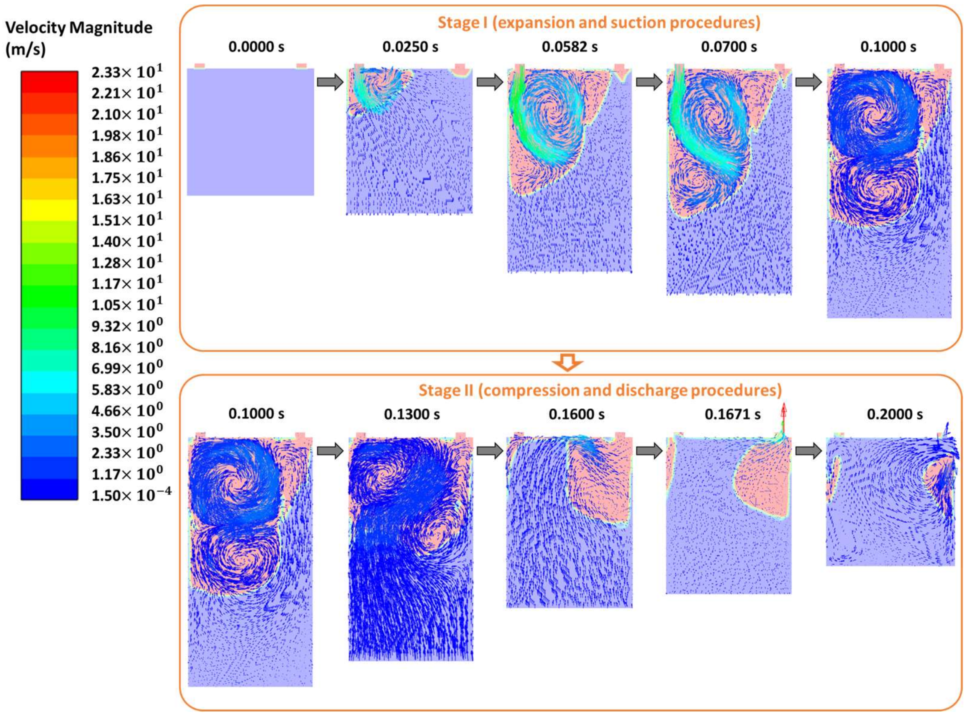

(b)

Figure 5. Results of the (**a**) volume fraction field and (**b**) velocity field (density of the ionic liquid: 1150 kg/m^3).

The results of the transient simulation with the liquid density of 1300 kg/m^3 are presented in Figure 6. It can be seen that at the time of 0.0250 s, the gas-occupied region was formed near the inlet with the expansion of the clearance volume near the outlet. At the time of 0.0596 s, a double-peak wave was observed when the gas-occupied region at the suction side was almost integrated with the discharge side. At the time of 0.0700 s, the gas-occupied region near the inlet and outlet space was combined. It was revealed that the space area on the wave peak located close to the discharge channel was larger than that in the cases of 1000 and 1150 kg/m^3 at the time of 0.0700 s. One droplet escaped from the adhered liquid on the cylinder wall at 0.0700 s. Three droplets were produced at 0.1000 s, the size of which was smaller compared to that in the simulations with the density of 1000 or 1150 kg/m^3. A neck-like structure was observed at the height of 50 mm (i.e., the original liquid level) due to the rotation of the largely derived vortex, the thickness of which was larger than that in the first two simulations. Only one liquid drop was found in the gas space in the compression chamber at 0.1300 s, the location of which was closer to the outlet region compared to that in the first two cases. At this time, the quantity of the remaining liquid adhered to the cylinder cover was smaller than in the first two simulations. Due to the reciprocating motion of the solid piston, the lump-like wave almost contacted the cylinder top at 0.1600 s, which is different from the first two cases. This means that with the increase in the liquid density, the liquid wave was promoted to contact the cylinder cover early in Stage II. It was also found that the ionic liquid occupied part of the discharge channel at 0.1680 s. Retention of hydrogen gas in the ionic liquid was observed when it was close to the end of Stage II. The largest velocity was found as 10.7 m/s at 0.0596 s in Stage I and 22.9 m/s at the time of 0.1680 s in Stage II.

The gas-liquid interaction in the hydrogen compressor under the liquid density of 1450 kg/m^3 is illustrated in Figure 7. It can be seen that at 0.0250 s, the gas-occupied region near the outlet and a sticktion of liquid on the chamber cover was observed, which blocked the connection of the gas space between the suction side and discharge side. The size of contacting area of the liquid on the chamber top was revealed smaller than that in the first three cases, which means that the elevation in the liquid density reduced the sticktion surface area of the liquid on the cover wall. The largest velocity in Stage I was found as 10.4 m/s at 0.0472 s, which was earlier than the first three simulations. At the time of 0.0700 s, the gas-occupied region at the suction side was observed integrated with the discharge side. The gas space near the outlet region was found larger compared to the first three cases. The droplet number at 0.0700 s was found as 1, which increased up to 3 at 0.1000 s. At the time of 0.1000 s, a slight neck phenomenon was found in the bulk liquid at the surface height of the original liquid column. The size of droplets was smaller than in the first three cases. It can be seen that at 0.1300 s, the biggest droplet almost contacted the liquid phase and adhered to the cylinder wall while the other two liquid drops had integrated into the ionic liquid. At the time of 0.1600 s, a contact of the lump-like wave with the compressor cover was revealed, which trapped the hydrogen gas around the inlet in the compression chamber. The highest velocity in Stage II was revealed as 21.7 m/s at 0.1767 s because the ionic liquid occupied the space of the outlet channel. The retention of hydrogen gas in the bulk liquid was found at the end of Stage II.

The simulation results with the density of ionic liquid of 1600 kg/m^3 are presented in Figure 8. At 0.0250 s, the gas space at the suction side was enlarged due to the suction of hydrogen gas. The size of the sticktion area of the liquid on the compressor cover was found smallest compared to the other four simulation cases at 0.0250 s. The largest velocity in Stage I occurred at 0.0474 s, which was found at 10.4 m/s. At this moment, the gas space at the suction side is not connected to the discharge side yet. At the time of 0.0700 s, the gas spaces at the suction and discharge sides are connected to each other when the wave with two peaks was also revealed. The gas space between the wavefront located close to the cylinder wall was found larger than the rest of the four cases. It can be concluded that the increase in the liquid density promoted the detachment of the liquid phase from the compressor cover during the suction procedure. One liquid drop started to be released from the ionic liquid adhered to the side wall of the cylinder at 0.0700 s while three droplets were produced at the time of 0.1000 s. The size of the droplet was the smallest of all the simulations. It means that the elevation in the liquid density would reduce the droplet size during the compression cycle. It can be seen in the snapshot at 0.1300 s that the droplets almost dissipated before they transferred into the bulk liquid phase. At 0.1600 s, a contact from the liquid wave of the compressor cover was observed when the wave moved upward. It is also illustrated in Figure 8b that two derived gas vortexes started to form at 0.0474 s. The dimension of these gas vortexes increased with time in Stage I. It can be observed that the size of the derived gas vortex slightly reduced with the increase in the liquid density. The highest velocity in State II was obtained as 22.6 m/s at 0.1757 s when the ionic liquid flowed out of the compressor cylinder accompanied by the hydrogen.

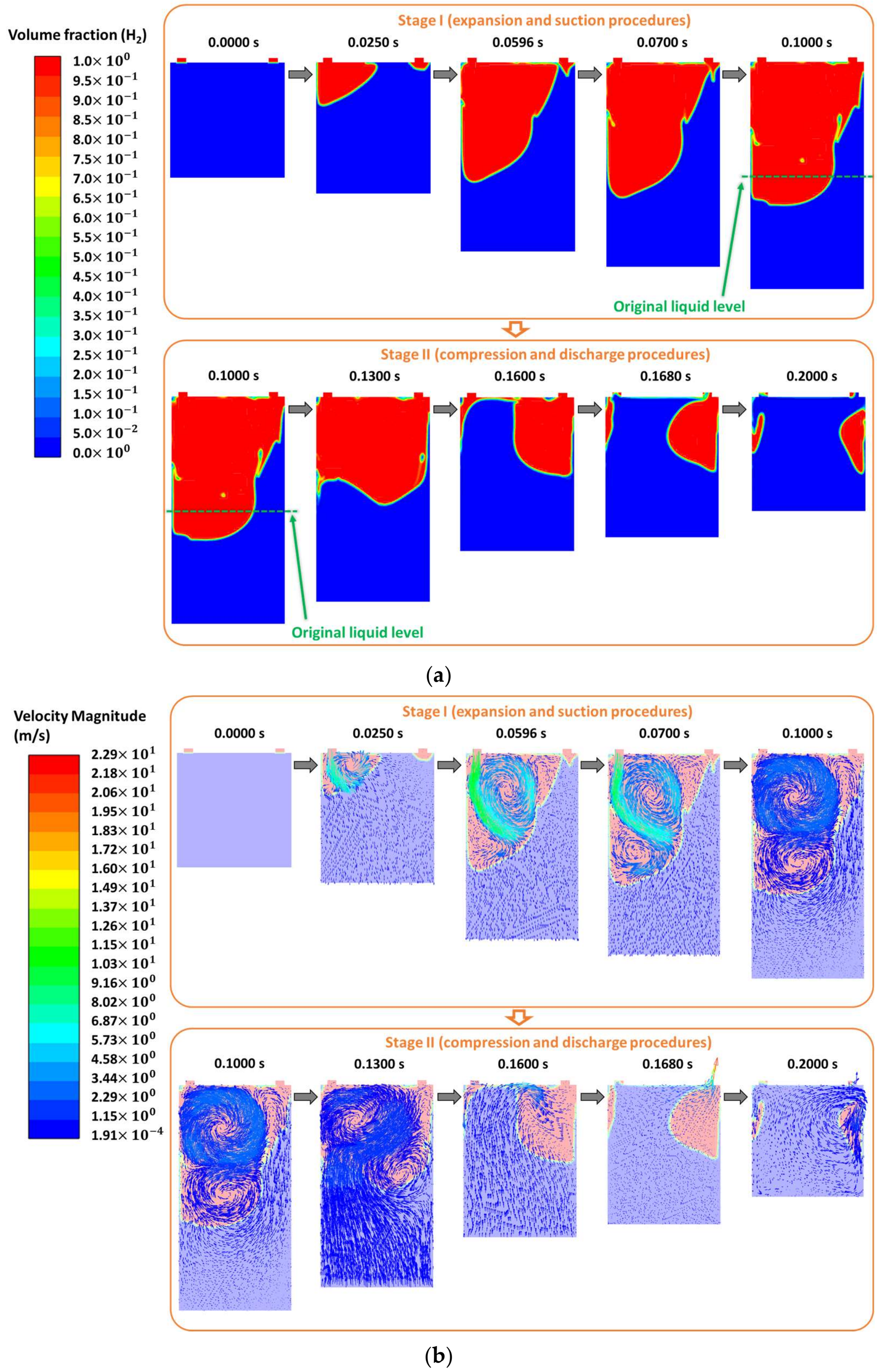

Figure 6. Results of the (**a**) volume fraction distribution and (**b**) velocity distribution (density of the ionic liquid: 1300 kg/m^3).

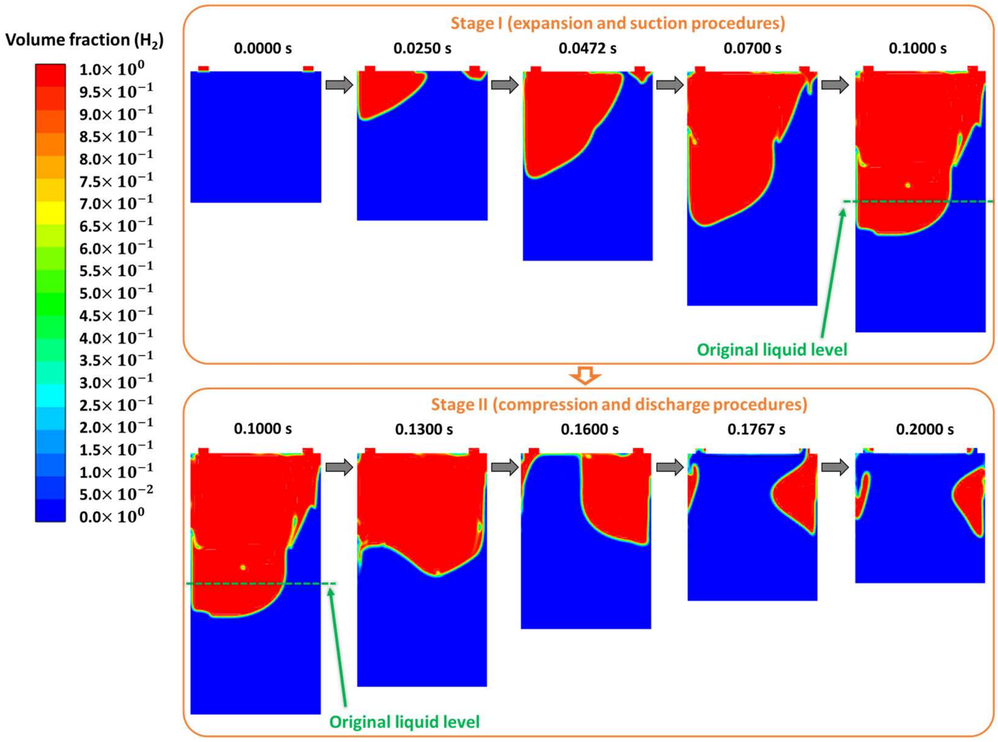

(**a**)

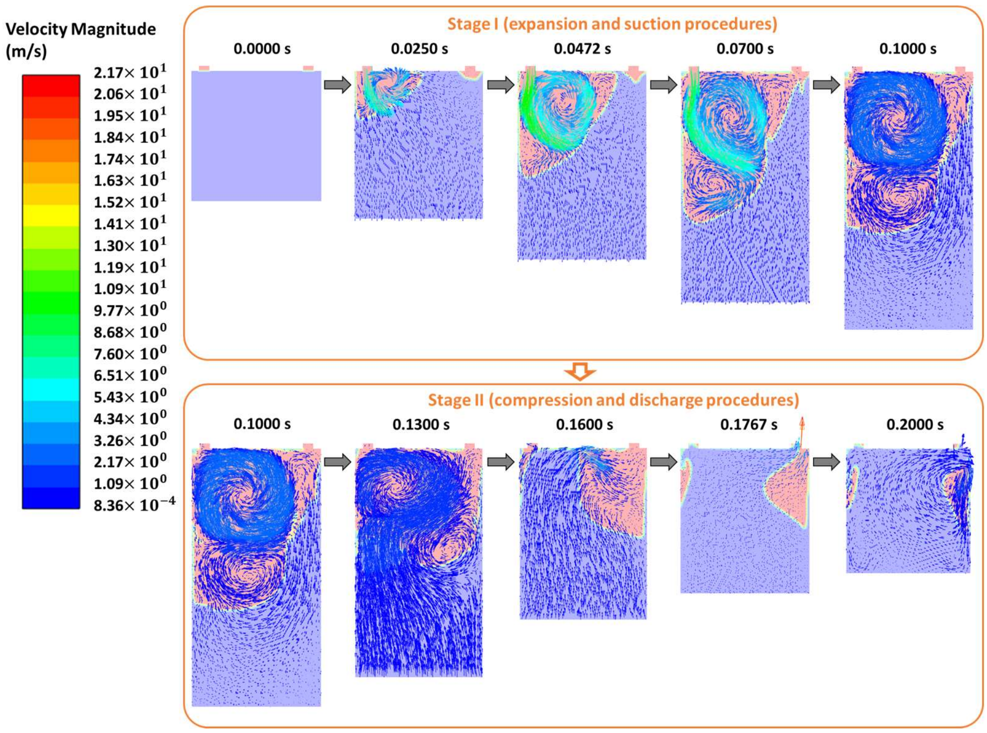

(**b**)

Figure 7. Results of the (**a**) volume fraction distribution and (**b**) velocity distribution (density of the ionic liquid: 1450 kg/m^3).

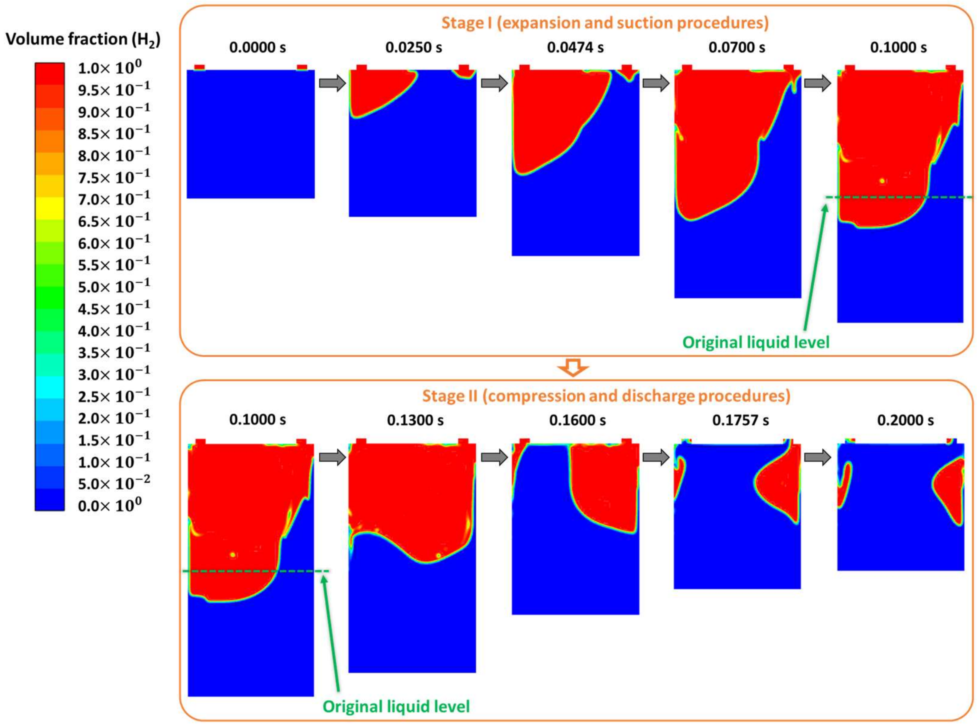

(**a**)

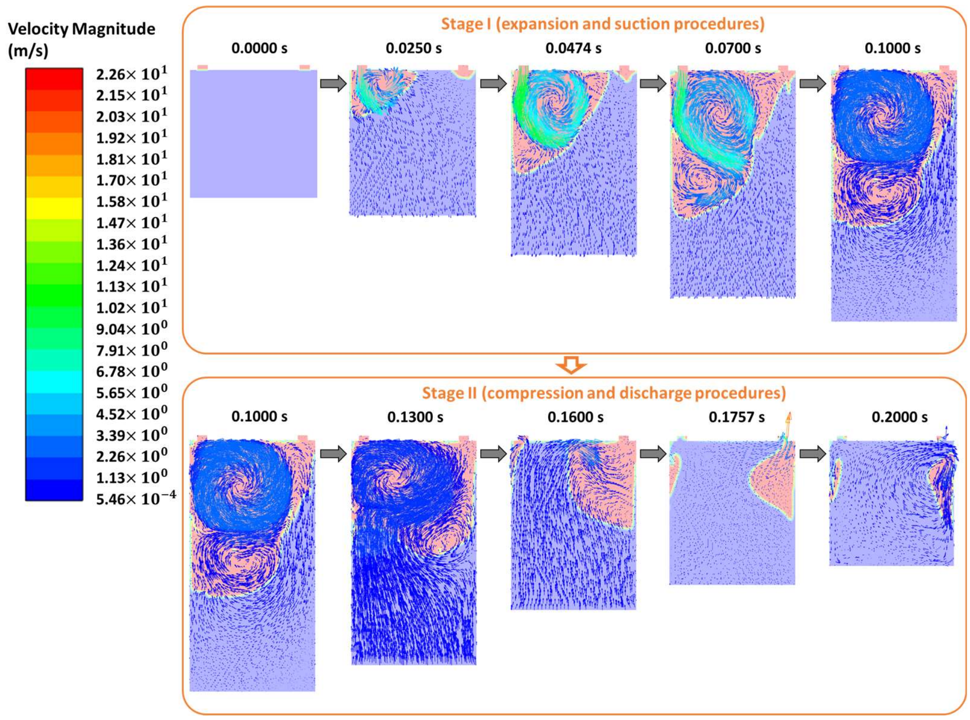

(**b**)

Figure 8. Results of the (**a**) volume fraction distribution and (**b**) velocity distribution (density of the ionic liquid: 1600 kg/m^3).

The transferred mass through the outlet during one entire operation cycle with different liquid densities is summarized in Figure 9. As presented in Figure 9a, with the increase in the liquid density, the transferred mass of the ionic liquid rose from 10.22 to 14.57 g. The growing speed of the mass transfer of the ionic liquid from 1000 to 1150 kg/m^3 was found to be higher than the rest. When the density was higher than 1150 kg/m^3, it showed a linear increase in the transferred mass of ionic liquid with an enlargement in the liquid density. Figure 9b shows that the mass of the hydrogen transferred via the outlet decreased first when the density of the ionic liquid elevated from 1000 to 1150 kg/m^3, and then a rise was found from 1150 to 1600 kg/m^3. The lowest value of the transferred mass for hydrogen was found at 0.609 g, while the highest was obtained at 0.636 g under the density of 1600 kg/m^3.

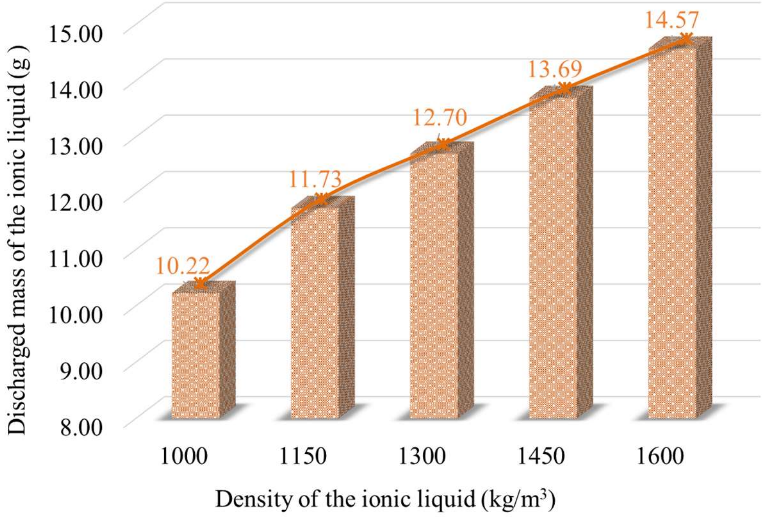

(**a**)

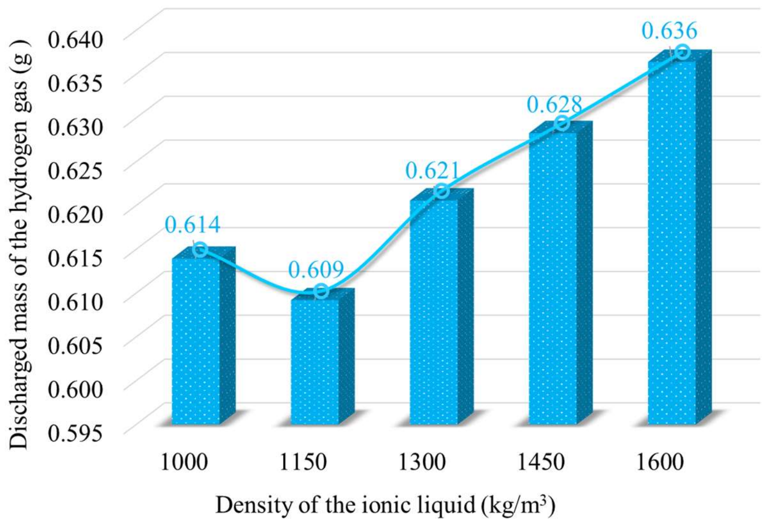

(**b**)

Figure 9. Mass transfer of (**a**) the ionic liquid and (**b**) hydrogen gas after one operation cycle.

The total turbulent kinetic energy with different densities of the ionic liquid in one operation cycle is provided in Figure 10. The turbulent kinetic energy is the mean kinetic energy per unit mass associated with eddies in a turbulent flow, and the total turbulent kinetic energy is the turbulent kinetic energy multiplied by the total mass of the fluids. A decrease in the total turbulent kinetic energy was found from 0.000 to 0.025 s, while an elevation in it was found from 0.025 to 0.075 s in all simulation cases. From 0.075 to 0.160 s, a general reduction in the total turbulent kinetic energy was revealed with small fluctuations when it was close to 0.160 s. The largest peak value was found as 0.61 kJ with a liquid density of 1000 kg/m^3, followed by the 0.60 kJ under the density of 1150 kg/m^3, while the lowest was found at 0.55 kJ in the case with a liquid density of 1600 kg/m^3. The value of the turbulent kinetic energy indicates the intensity of flow turbulence, which assists to identify the instability of the flow. This flow motion energy generated from the eddy interaction converts the input kinetic energy into the thermal term, which should be suppressed in the compressor. Therefore, a density in the range of 1300–1450 kg/m^3 is the optimal density of the ionic liquid for designing the compressor with requirements provided in this study considering the gas-liquid interaction, transferred mass via the outlet, and the total turbulent kinetic energy. It is worth noting that the results of optimal density may vary with different design requirements. However, the calculation methods and design progress provided in this paper can be applied to the design of the ionic liquid compressor at different operating conditions.

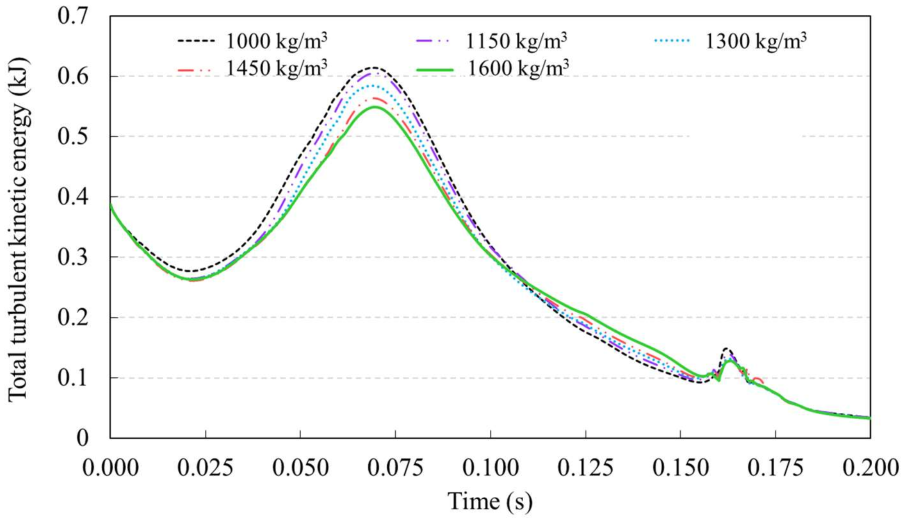

Figure 10. Total turbulent kinetic energy in one operation cycle with time and with different liquid densities.

5. Conclusions

This study proposed the design methodology for selecting the optimal liquid density for compressing the hydrogen gas. The transit gas-liquid interaction is analyzed through numerical simulations under varied liquid density values. The main conclusions drawn from this paper are shown as follows.

- The area of the gas-occupied region above the wave peak during the suction procedure enlarged when the liquid density increased. The size of droplets generated in the hydrogen gas suction procedure reduced with the increase in the liquid density. The dimension of the derived gas vortex slightly decreased when the liquid density rose.
- The neck-like structure of the liquid column was observed at the original liquid level at the time of 0.1000 s, the thickness of which rose with the elevation in the liquid density. At the time of 0.1300 s, the remaining liquid on the surface of the compressor cover reduced with the increase in the liquid density.
- The increase in the liquid density promoted the detachment of the ionic liquid from the compressor cover in Stage I and the contact from the liquid wave of the compressor cover early in Stage II.
- The mass transfer of the ionic liquid after one operation cycle continually rose when the liquid density increased. The transferred mass of the hydrogen gas after one operation cycle decreased first and then increased with the elevation in the liquid density with the trough at 1150 kg/m^3.
- The total turbulent kinetic energy was found with the largest peak value of 0.61 kJ with a liquid density of 1000 kg/m^3 and the lowest value of 0.55 kJ in the simulation with a liquid density of 1600 kg/m^3.

- The liquid density in the range of 1300–1450 kg/m^3 is suggested for designing the hydrogen compressor adopting the ionic liquid piston with the design requirements provided considering the gas-liquid interaction, the mass transfer via the outlet, and the total turbulent kinetic energy.

For design conditions different from this study, the optimal values can be different, but the design methodology and calculation methods are still valid for the design of the ionic liquid compressor.

Author Contributions: Conceptualization, Y.G. and X.P.; methodology, Y.G. and J.F.; software, Q.W.; validation, Q.W. and M.G.; formal analysis, Q.W.; investigation, M.G.; data curation, J.F.; writing-original draft preparation, Y.G.; writing-review and editing, X.P. and J.F.; visualization, Y.G. and Q.W.; supervision, X.P.; funding acquisition, Y.G. All authors have read and agreed to the published version of the manuscript.

Funding: This research was funded by the National Natural Science Foundation of China, grant number. 52006174, and Open Foundation of State Key Laboratory of Compressor Technology, grant number. SKL-YSJ201901.

Data Availability Statement: The data presented in this study are available on request from the corresponding authors. The data are not publicly available due to privacy.

Conflicts of Interest: The authors declare that the research was conducted in the absence of any commercial or financial relationships that could constitute a potential conflict of interest.

References

1. Isaac, N.; Saha, A.K. A Review of the Optimization Strategies and Methods Used to Locate Hydrogen Fuel Refueling Stations. *Energies* **2023**, *16*, 2171. [CrossRef]
2. Lamagna, M.; Ferrario, A.M.; Astiaso Garcia, D.; McPhail, S.; Comodi, G. Reversible solid oxide cell coupled to an offshore wind turbine as a poly-generation energy system for auxiliary backup generation and hydrogen production. *Energy Rep.* **2022**, *8*, 14259–14273. [CrossRef]
3. Dall'Armi, C.; Pivetta, D.; Taccani, R. Hybrid PEM Fuel Cell Power Plants Fuelled by Hydrogen for Improving Sustainability in Shipping: State of the Art and Review on Active Projects. *Energies* **2023**, *16*, 2022. [CrossRef]
4. Giacoppo, G.; Trocino, S.; Lo Vecchio, C.; Baglio, V.; Díez-García, M.I.; Aricò, A.S.; Barbera, O. Numerical 3D Model of a Novel Photoelectrolysis Tandem Cell with Solid Electrolyte for Green Hydrogen Production. *Energies* **2023**, *16*, 1953. [CrossRef]
5. Gultom, N.S.; Abdullah, H.; Kuo, D.-H. Facile synthesis of cobalt-doped (Zn,Ni) (O,S) as an efficient photocatalyst for hydrogen production. *J. Energy Inst.* **2019**, *92*, 1428–1439. [CrossRef]
6. Matamba, T.; Iglauer, S.; Keshavarz, A. A progress insight of the formation of hydrogen rich syngas from coal gasification. *J. Energy Inst.* **2022**, *105*, 81–102. [CrossRef]
7. Li, H.; Cao, X.; Liu, Y.; Shao, Y.; Nan, Z.; Teng, L.; Peng, W.; Bian, J. Safety of hydrogen storage and transportation: An overview on mechanisms, techniques, and challenges. *Energy Rep.* **2022**, *8*, 6258–6269. [CrossRef]
8. Fang, J.; Yin, X.; Wang, A.; Sun, X.; Liu, Y.; Cao, F. Cooling performance enhancement for the automobile transcritical CO_2 air conditioning system with various internal heat exchanger effectiveness. *Appl. Therm. Eng.* **2021**, *196*, 117274. [CrossRef]
9. Raeesi, M.; Changizian, S.; Ahmadi, P.; Khoshnevisan, A. Performance analysis of a degraded PEM fuel cell stack for hydrogen passenger vehicles based on machine learning algorithms in real driving conditions. *Energy Convers. Manag.* **2021**, *248*, 114793. [CrossRef]
10. Gallo, M.; Marinelli, M. The Use of Hydrogen for Traction in Freight Transport: Estimating the Reduction in Fuel Consumption and Emissions in a Regional Context. *Energies* **2023**, *16*, 508. [CrossRef]
11. Al-Mukainah, H.; Al-Yaseri, A.; Yekeen, N.; Hamad, J.A.; Mahmoud, M. Wettability of shale–brine–H2 system and H2-brine interfacial tension for assessment of the sealing capacities of shale formations during underground hydrogen storage. *Energy Rep.* **2022**, *8*, 8830–8843. [CrossRef]
12. Hazrat, M.A.; Rasul, M.G.; Jahirul, M.I.; Chowdhury, A.A.; Hassan, N.M.S. Techno-economic analysis of recently improved hydrogen production pathway and infrastructure. *Energy Rep.* **2022**, *8*, 836–844. [CrossRef]
13. Rufer, A. Increasing the Energy Efficiency of Gas Boosters for Hydrogen Storage and for Refueling Stations. *Energies* **2023**, *16*, 1763. [CrossRef]
14. Mazloomi, K.; Gomes, C. Hydrogen as an energy carrier: Prospects and challenges. *Renew. Sustain. Energy Rev.* **2012**, *16*, 3024–3033. [CrossRef]
15. Rivard, E.; Trudeau, M.; Zaghib, K. Hydrogen Storage for Mobility: A Review. *Materials* **2019**, *12*, 1973. [CrossRef]
16. Wang, L.; Jiao, S.; Xie, Y.; Xia, S.; Zhang, D.; Zhang, Y.; Li, M. Two-way dynamic pricing mechanism of hydrogen filling stations in electric-hydrogen coupling system enhanced by blockchain. *Energy* **2022**, *239*, 122194. [CrossRef]

17. Caponi, R.; Monforti Ferrario, A.; Del Zotto, L.; Bocci, E. Hydrogen refueling stations and fuel cell buses four year operational analysis under real-world conditions. *Int. J. Hydrogen Energy* **2022**. [CrossRef]
18. Berstad, D.; Gardarsdottir, S.; Roussanaly, S.; Voldsund, M.; Ishimoto, Y.; Nekså, P. Liquid hydrogen as prospective energy carrier: A brief review and discussion of underlying assumptions applied in value chain analysis. *Renew. Sustain. Energy Rev.* **2022**, *154*, 111772. [CrossRef]
19. Amirthan, T.; Perera, M.S.A. The role of storage systems in hydrogen economy: A review. *J. Nat. Gas Sci. Eng.* **2022**, *108*, 104843. [CrossRef]
20. Ahsan, N.; Al Rashid, A.; Zaidi, A.A.; Imran, R.; Abdul Qadir, S. Performance analysis of hydrogen fuel cell with two-stage turbo compressor for automotive applications. *Energy Rep.* **2021**, *7*, 2635–2646. [CrossRef]
21. Abdalla, A.M.; Hossain, S.; Nisfindy, O.B.; Azad, A.T.; Dawood, M.; Azad, A.K. Hydrogen production, storage, transportation and key challenges with applications: A review. *Energy Convers. Manag.* **2018**, *165*, 602–627. [CrossRef]
22. Li, X.; Chen, J.; Wang, Z.; Jia, X.; Peng, X. A non-destructive fault diagnosis method for a diaphragm compressor in the hydrogen refueling station. *Int. J. Hydrogen Energy* **2019**, *44*, 24301–24311. [CrossRef]
23. Arjomand Kermani, N.; Petrushina, I.; Rokni, M.M. Evaluation of ionic liquids as replacements for the solid piston in conventional hydrogen reciprocating compressors: A review. *Int. J. Hydrogen Energy* **2020**, *45*, 16337–16354. [CrossRef]
24. Białek, P.; Bielawski, P. Failure analysis of refinery hydrogen reciprocating compressors. *Diagnostyka* **2018**, *19*, 83–92. [CrossRef]
25. Charbonnier, V.; Enoki, H.; Asano, K.; Kim, H.; Sakaki, K. Tuning the hydrogenation properties of $Ti_{1+y}Cr_{2-x}Mn_x$ laves phase compounds for high pressure metal-hydride compressors. *Int. J. Hydrogen Energy* **2021**, *46*, 36369–36380. [CrossRef]
26. Sdanghi, G.; Nicolas, V.; Mozet, K.; Schaefer, S.; Maranzana, G.; Celzard, A.; Fierro, V. A 70 MPa hydrogen thermally driven compressor based on cyclic adsorption-desorption on activated carbon. *Carbon* **2020**, *161*, 466–478. [CrossRef]
27. Hu, Y.; Xu, X.; Wang, W. A new cavity profile for a diaphragm compressor used in hydrogen fueling stations. *Int. J. Hydrogen Energy* **2017**, *42*, 24458–24469. [CrossRef]
28. Ren, S.; Jia, X.; Jiang, J.; Zhang, S.; Zhao, B.; Peng, X. Effect of hydraulic oil compressibility on the volumetric efficiency of a diaphragm compressor for hydrogen refueling stations. *Int. J. Hydrogen Energy* **2022**, *47*, 15224–15235. [CrossRef]
29. Wang, T.; Jia, X.; Li, X.; Ren, S.; Peng, X. Thermal-structural coupled analysis and improvement of the diaphragm compressor cylinder head for a hydrogen refueling station. *Int. J. Hydrogen Energy* **2020**, *45*, 809–821. [CrossRef]
30. Peng, Z.; Li, Q.; Ouyang, L.; Jiang, W.; Chen, K.; Wang, H.; Liu, J.; Li, Z.; Wang, S.; Zhu, M. Overview of hydrogen compression materials based on a three-stage metal hydride hydrogen compressor. *J. Alloy. Compd.* **2022**, *895*, 162465. [CrossRef]
31. Gray, E.M. Alloy selection for multistage metal-hydride hydrogen compressors: A thermodynamic model. *Int. J. Hydrogen Energy* **2021**, *46*, 15702–15715. [CrossRef]
32. Gkanas, E.I.; Stamatakis, E.; Christodoulou, C.N.; Tzamalis, G.; Karagiorgis, G.; Chroneos, A.; Kuganathan, N.; Khzouz, M.; Stubos, A.K. Study on the operation and energy demand of dual-stage Metal Hydride Hydrogen Compressors under effective thermal management. *Int. J. Hydrogen Energy* **2021**, *46*, 29272–29287. [CrossRef]
33. Zhou, H.; Dong, P.; Zhu, S.; Li, S.; Zhao, S.; Wang, Y. Design and theoretical analysis of a liquid piston hydrogen compressor. *J. Energy Storage* **2021**, *41*, 102861. [CrossRef]
34. Guo, Y.; Wang, T.; Liu, X.; Zhang, M.; Peng, X. Mathematical modelling and design of the ionic liquid compressor for the hydrogen refuelling station. *Int. J. Energy Res.* **2022**, *46*, 19123–19137. [CrossRef]
35. Ventura, S.P.M.; e Silva, F.A.; Quental, M.V.; Mondal, D.; Freire, M.G.; Coutinho, J.A.P. Ionic-Liquid-Mediated Extraction and Separation Processes for Bioactive Compounds: Past, Present, and Future Trends. *Chem. Rev.* **2017**, *117*, 6984–7052. [CrossRef]
36. Lim, J.R.; Chua, L.S.; Mustaffa, A.A. Ionic liquids as green solvent and their applications in bioactive compounds extraction from plants. *Process Biochem.* **2022**, *122*, 292–306. [CrossRef]
37. Hajipour, A.R.; Rafiee, F. Recent Progress in Ionic Liquids and their Applications in Organic Synthesis. *Org. Prep. Proced. Int.* **2015**, *47*, 249–308. [CrossRef]
38. Merone, M.G.; Tartaglia, A.; Rosato, E.; D'Ovidio, C.; Kabir, A.; Ulusoy, I.H.; Savini, F.; Locatelli, M. Ionic Liquids in Analytical Chemistry: Applications and Recent Trends. *Curr. Anal. Chem.* **2021**, *17*, 1340–1355. [CrossRef]
39. Ali, S.A.; Mulk, W.U.; Ullah, Z.; Khan, H.; Zahid, A.; Shah, M.U.H.; Shah, S.N. Recent Advances in the Synthesis, Application and Economic Feasibility of Ionic Liquids and Deep Eutectic Solvents for CO_2 Capture: A Review. *Energies* **2022**, *15*, 9098. [CrossRef]
40. Kreivaitis, R.; Kupčinskas, A.; Žunda, A.; Ta, T.N.; Horng, J.H. Effect of temperature on the lubrication ability of two ammonium ionic liquids. *Wear* **2022**, *492–493*, 204217. [CrossRef]
41. Ding, H.; Ye, W.; Wang, Y.; Wang, X.; Li, L.; Liu, D.; Gui, J.; Song, C.; Ji, N. Process intensification of transesterification for biodiesel production from palm oil: Microwave irradiation on transesterification reaction catalyzed by acidic imidazolium ionic liquids. *Energy* **2018**, *144*, 957–967. [CrossRef]
42. Kazemi, S.; Nor, M.I.M.; Teoh, W.H. Thermodynamic and economic investigation of an ionic liquid as a new proposed geothermal fluid in different organic Rankine cycles for energy production. *Energy* **2020**, *193*, 116722. [CrossRef]
43. Kazmi, B.; Haider, J.; Ammar Taqvi, S.A.; Qyyum, M.A.; Ali, S.I.; Hussain Awan, Z.U.; Lim, H.; Naqvi, M.; Naqvi, S.R. Thermodynamic and economic assessment of cyano functionalized anion based ionic liquid for CO_2 removal from natural gas integrated with, single mixed refrigerant liquefaction process for clean energy. *Energy* **2022**, *239*, 122425. [CrossRef]
44. Kalita, P.; Lukaszewicz, G. *Navier-Stokes Equations: An Introduction with Applications*, 1st ed.; Springer Nature Customer Service Center GmbH: London, UK, 2016.

45. Nangia, N.; Griffith, B.E.; Patankar, N.A.; Bhalla, A.P.S. A robust incompressible Navier-Stokes solver for high density ratio multiphase flows. *J. Comput. Phys.* **2019**, *390*, 548–594. [CrossRef]
46. Lee, J.; Ahn, Y.; Kim, Y. Experimental study on effect of density ratio and phase transition during sloshing impact in rectangular tank. *Ocean. Eng.* **2021**, *242*, 110105. [CrossRef]
47. Rao, Y.; Liu, C.; Wang, H.; Ni, Y.; Lv, C.; Liu, S.; Lan, Y.; Wang, S. Density ratio effect on particle sedimentation in a vertical channel. *Chin. J. Phys.* **2018**, *56*, 1427–1438. [CrossRef]
48. Troncoso, J.; Cerdeiriña, C.A.; Sanmamed, Y.A.; Romaní, L.; Rebelo, L.P.N. Thermodynamic Properties of Imidazolium-Based Ionic Liquids: Densities, Heat Capacities, and Enthalpies of Fusion of [bmim][PF6] and [bmim][NTf2]. *J. Chem. Eng. Data* **2006**, *51*, 1856–1859. [CrossRef]
49. Lazzús, J. Estimation of Density as a Function of Temperature and Pressure for Imidazolium-Based Ionic Liquids Using a Multilayer Net with Particle Swarm Optimization. *Int. J. Thermophys.* **2009**, *30*, 883–909. [CrossRef]
50. Gardas, R.L.; Freire, M.G.; Carvalho, P.J. High-Pressure Densities and Derived Thermodynamic Properties of Imidazolium-Based Ionic Liquids. *J. Chem. Eng. Data* **2007**, *52*, 80–88. [CrossRef]
51. Tomé, L.I.N.; Carvalho, P.J.; Freire, M.G.; Marrucho, I.M.; Fonseca, I.M.A.; Ferreira, A.G.M.; Coutinho, J.A.P.; Gardas, R.L. Measurements and Correlation of High-Pressure Densities of Imidazolium-Based Ionic Liquids. *J. Chem. Eng. Data* **2008**, *53*, 1914–1921. [CrossRef]
52. Fredlake, C.P.; Crosthwaite, J.M.; Hert, D.G.; Aki, S.N.V.K.; Brennecke, J.F. Thermophysical Properties of Imidazolium-Based Ionic Liquids. *J. Chem. Eng. Data* **2004**, *49*, 954–964. [CrossRef]
53. Kermani, N.A.; Petrushina, I.; Nikiforov, A.; Jensen, J.O.; Rokni, M. Corrosion behavior of construction materials for ionic liquid hydrogen compressor. *Int. J. Hydrogen Energy* **2016**, *41*, 16688–16695. [CrossRef]